arXiv:1801.06693v4 [math.NA] 30 Aug 2018

Real-time photoacoustic projection imaging using deep learning

Johannes Schwab[1], Stephan Antholzer[1], Robert Nuster[2], and Markus Haltmeier[1,*]

[1]Department of Mathematics, University of Innsbruck, Technikerstraße 13, 6020 Innsbruck, Austria
[2]Department of Physics, Karl-Franzens-Universitaet Graz, Universitaetsplatz 5, 8010 Graz, Austria
[*]Corresponding author: markus.haltmeier@uibk.ac.at

August 30, 2018

Abstract

Photoacoustic tomography (PAT) is an emerging and non-invasive hybrid imaging modality for visualizing light absorbing structures in biological tissue. The recently invented PAT systems using arrays of 64 parallel integrating line detectors allow capturing photoacoustic projection images in fractions of a second. Standard image formation algorithms for this type of setup suffer from under-sampling due to the sparse detector array, blurring due to the finite impulse response of the detection system, and artifacts due to the limited detection view. To address these issues, in this paper we develop a new direct and non-iterative image reconstruction framework using deep learning. The proposed DALnet combines the universal backprojection (UBP) using dynamic aperture length (DAL) correction with a deep convolutional neural network (CNN). Both subnetworks contain free parameters that are adjusted in the training phase. As demonstrated by simulation and experiment, the DALnet is capable of producing high-resolution projection images of 3D structures at a frame rate of over 50 images per second on a standard PC with NVIDIA TITAN Xp GPU. The proposed network is shown to outperform state-of-the-art iterative total variation reconstruction algorithms in terms of reconstruction speed as well as in terms of various evaluation metrics.

1 Introduction

Photoacoustic tomography (PAT) beneficially combines the high contrast of pure optical imaging and the high spatial resolution of pure ultrasound imaging [1, 2]. The basic principle of PAT is as follows. A semitransparent sample (such as parts of a human patient) is illuminated with short pulses of optical radiation. A fraction of the optical energy is absorbed inside the sample which causes thermal heating, expansion, and a subsequent acoustic pressure wave depending on the interior light absorbing structures. The acoustic pressure is measured outside of the sample and used to reconstruct an image of its interior. The standard approach for detecting the acoustic waves in PAT is to use small piezoelectric detector elements arranged on a surface around the object. In the recent years, PAT systems using integrating line detectors have been invented and shown to be a high-resolution alternative to the classical approach of using approximate point detectors. Within such systems the pressure signals are integrated along the dimension of the line detectors from which 2D projections of the 3D source can be reconstructed [3, 4]. By collecting 2D projections from different directions, a 3D image of the PA source can be recovered with the 2D inverse Radon transform [5, 6, 7].

As the fabrication of an array of parallel line detectors is challenging, initial experiments for integrating line detectors have been carried out using a single line sensor that is sequentially moved around the sample in order to collect sufficient data. Recently, PAT systems made of arrays with up to 64 parallel line detectors have been realized [8, 9, 10, 11] allowing real time PA projection imaging of 3D structures. The number of line detectors influences the spatial resolution of the measured data and therefore, the spatial resolution of the final reconstruction. To increase the spatial resolution, the whole measurement process can be repeated for different detector locations. This, however, again increases the measurement time. If the number of detector locations is far below the Nyquist rate, standard image reconstruction algorithms (such as filtered backprojection) yield low quality images containing streak-like under-sampling artifacts. Consequently, high spatial resolution would require increasing the number of line sensors. In order to address the spatial under-sampling, compressed sensing techniques for PAT have been developed [12, 13, 14, 15, 16]. These methods require time-consuming iterative image reconstruction algorithms and, additionally, assume a sparsity prior that is not always strictly satisfied [13]. Besides under-sampling artefacts, reconstruction with standard algorithms additionally suffers from limited data artifacts as well as blurring due to the impulse response function (IRF) of the sensor elements.

To address the above issues, in this paper we develop new non-iterative image

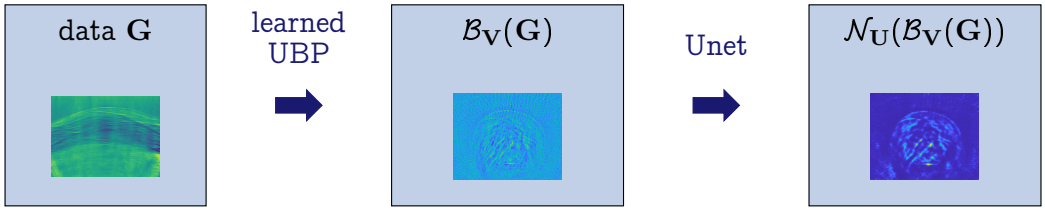


Figure 1: **Schematic illustration of the DALnet.** The proposed network consist of a backprojection layer with DAL correction and a subsequent CNN. Both subnetworks contain free parameters and the DALnet is trained end-to-end.

reconstruction algorithms based on deep learning that are able to deal with non-ideal IRF, spatial under-sampling and the limited view issue. We establish a network combining the universal backprojection (UBP) with dynamic aperture length (DAL) correction [17, 18] to address the limited view issue and the IRF with a convolutional neural network (CNN) to address spatial under-sampling. The resulting DALnet contains free parameters from the UBP layer and the CNN part which both are adjusted end-to-end during the so-called training phase; see Figure 1. For sparse sampling PAT, image reconstruction with CNNs has first been proposed in [19], where, however, neither the limited view nor the finite bandwidth IRF have been considered. Learned filter kernels have be considered for x-ray CT in [20]. CNNs have been previously applied to other medical imaging modalities such as (CT) and magnetic resonance imaging (MRI) [21, 22, 23, 24, 25, 26, 27, 28]. (For different network architectures used in PAT and other tomographic problems see, for example, [29, 30, 31, 32, 33, 34, 35, 36, 37].) However, in all these approaches only the CNN part contains trainable weights, whereas the proposed DALnet contains trainable weights in the UBP layer and the CNN part.

We train the proposed DALnet for the PA 64-line detector array system developed in [10] and thereby also account for finite IRF and the limited view issue. The algorithm is tested on an experimental data set consisting of several PA projection images of a finger of one of the authors. We demonstrate that real-time high-resolution PA projection imaging is possible with the trained DALnet. The proposed method is compared with the FBP algorithm as well as state-of-the-art iterative image reconstruction algorithms using total variation (TV) with and without positivity constraint. Our results demonstrate that the DALnet outperforms TV-minimization in terms of reconstruction speed as well as in various error metrics evaluated on test data not contained in the training set.

2 Background

2.1 Photoacoustic tomography (PAT)

Suppose some sample of interest is uniformly illuminated with a short optical pulse which induces an acoustic pressure wave originating at light absorbing structures of the sample. Assuming constant speed of sound and instantaneous heating, the induced acoustic pressure satisfies the free space wave equation

$$\partial_t^2 p(\boldsymbol{r}, t) - v_s^2 \, \Delta_r p(\boldsymbol{r}, t) = \delta'(t) \, f(\boldsymbol{r}) \, . \tag{1}$$

Here $\boldsymbol{r} \in \mathbb{R}^d$ is the spatial location, $t \in \mathbb{R}$ the time, Δ_r the spatial Laplacian, and v_s the speed of sound. The wave equation is augmented with initial condition $p(\boldsymbol{r}, t) = 0$ for $t < 0$, in which case the acoustic pressure is uniquely defined by (1). The PA source $f(\boldsymbol{r})$ is assumed to vanish outside a bounded region $\boldsymbol{D} \subseteq \mathbb{R}^d$ and has to be recovered from measurements of the acoustic pressure outside the sample.

Both cases $d = 2, 3$ for the spatial dimension are relevant in PAT. The case $d = 3$ arises in PAT using classical point-wise measurements and the case $d = 2$ for PAT with integrating line detectors. In this work we consider PAT with integrating line detectors and the 2D wave equation. The PA source is then a projection image of the 3D source. Full 3D image reconstruction can be performed by combining projection images from different directions using the 2D inverse Radon transform [3, 4, 5, 6, 7]. However, the PA projection images itself are already of valuable diagnostic use.

With any PA system, the acoustic pressure can only be measured at a finite number of detector locations, each having limited bandwidth IRF $\boldsymbol{\phi}$ and recording a finite number of temporal samples. This yields to the PAT image reconstruction problem of reconstructing $\mathbf{F}$ from data

$$\mathbf{G}[m] = (\mathcal{A}(\mathbf{F}) *_t \boldsymbol{\phi})[m] + \boldsymbol{\xi}[m] \quad \text{for } m \in \{1, \dots, M_s\} \times \{1, \dots, M_t\} \, . \tag{2}$$

Here $\mathbf{F} \in \mathbb{R}^{N_r \times N_r}$ is the discretized PA source, $\mathcal{A} \colon \mathbb{R}^{N_r \times N_r} \to \mathbb{R}^{M_s \times M_t}$ the discretization of the solution operator of the wave equation evaluated at the detector locations, $\boldsymbol{\phi}$ is the discrete IRF and $\boldsymbol{\xi} \in \mathbb{R}^{M_s \times M_t}$ models the noise in the data. The product $N_r \times N_r$ is the number of reconstruction points, M_s the number of detector locations and M_t the number of temporal samples. The IRF of the detection system (besides other physical factors such as attenuation and finite optical pulse duration) limits the spatial resolution and therefore dictate the number of reconstruction points [38, 39]. The temporal sampling rate $1/M_t$ is well above the Nyquist sampling rate governed by physical resolution. However, the number of detector locations is limited in

practical applications. Using linear reconstruction algorithms, the number M_s is thereby directly related to the resolution of the final reconstruction [40].

2.2 Universal backprojection

In the idealized situation of continuous sampling and full view where the pressure data $p(\boldsymbol{s}, t)$ are known on the whole boundary $\partial \boldsymbol{D}$, and assuming an ideal IRF $\phi(t) = \delta(t)$ (the Dirac delta function) of the detection system, the inverse problem of recovering the PA source is uniquely and stably solvable. Several efficient and robust methods including filtered backprojection (FBP), time reversal, or Fourier methods are available [41, 42, 43, 44, 45, 46, 47, 48, 49, 50] . A particularly useful theoretically exact inversion method is the 2D universal backprojection (UBP)

$$(\mathcal{B}g)(\boldsymbol{r}) = \frac{1}{\pi} \int_{\partial \boldsymbol{D}} \Big(\boldsymbol{n}_{\boldsymbol{s}} \bullet (\boldsymbol{r} - \boldsymbol{s}) \int_{|\boldsymbol{r}-\boldsymbol{s}|}^{\infty} \frac{\partial_t t^{-1} g(\boldsymbol{s}, t)}{\sqrt{t^2 - |\boldsymbol{r} - \boldsymbol{s}|^2}} \, \mathrm{d}t \Big) \mathrm{d}\boldsymbol{s} \,. \tag{3}$$

Here g is the observed data on the detection curve $\boldsymbol{S}$, $\boldsymbol{r}$ is the reconstruction point, $\boldsymbol{s}$ the point on the detection curve, and $\boldsymbol{n}_{\boldsymbol{s}}$ the exterior normal to $\boldsymbol{S} \subseteq \partial \boldsymbol{D}$ with unit length.

The 2D UBP has been first derived in [51] where it is shown to be theoretically exact for linear and circular geometries, which means that the PA source f can be exactly recovered by the inversion formula $f = \mathcal{B}\mathcal{W}f$, where $\mathcal{W}f$ denotes the solution of (1) restricted to $\partial \boldsymbol{D} \times (0, \infty)$. The 3D version of the UBP has been first derived in [50] for planar, spherical and cylindrical geometry. In the recent years, the UBP has been shown to be theoretically exact for elliptical and other geometries in arbitrary dimensions [45, 46, 52, 47, 53].

2.3 Limited view problem and DAL correction

In most practical applications, PA data are available only on a proper subset $\boldsymbol{S} \subsetneq \partial \boldsymbol{D}$. To focus on the main ideas, let us assume that one can identify a so-called visible zone $\boldsymbol{D}_0 = \boldsymbol{D}_0(\boldsymbol{S})$ defined by the property that at least one of any two antipodal rays starting in the visible zone hits the detection curve $\boldsymbol{S}$; see Figure 2(a). The reconstruction of f is known to be stable within the visible zone; however, no direct and theoretically exact inversion method is available. In such a situation, one can apply iterative methods, where the forward and adjoint problem have to be solved repeatedly [54, 55, 56, 57]. This yields to an increased computation time compared to direct methods. Typically, the numerical complexity for solving the forward and

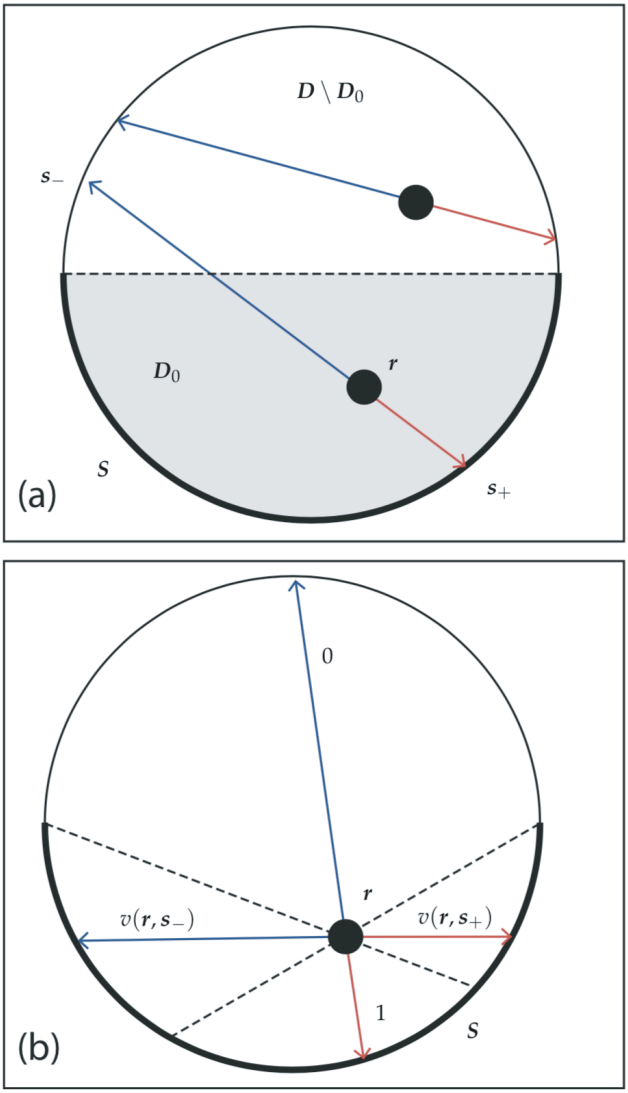


Figure 2: **Visible zone and UBP with DAL correction.** (a) Inside the visible zone $\boldsymbol{D}_0$ for any pair of rays pointing in opposite direction at least one of them hits the detection curve. (b) To address the limited view problem, the UBP with DAL correction includes a weight with $v(\boldsymbol{r}, \boldsymbol{s}_+) + v(\boldsymbol{r}, \boldsymbol{s}_-) = 1$. If $\boldsymbol{s}$ is located outside of $\boldsymbol{S}$, then $v(\boldsymbol{r}, \boldsymbol{s}) = 0$.

adjoint problem is $\mathcal{O}(N_r^3)$ which is the same as one application of the UBP. For planar geometries Fourier methods are available where the forward and adjoint problem (as well as the UBP) can be evaluated with $\mathcal{O}(N_r^2 \log N_r)$ operation counts.

Another approach, which is computationally less expensive than iterative methods, is to adapt the UBP to the limited view data. For full data, any reconstruction point in the UBP (3) receives information from two antipodal

points $\boldsymbol{s}_+$ and $\boldsymbol{s}_-$. In the limited data case, some directions have missing antipodal points which yields to blurring of the reconstruction. To account for this issue, in [17] the dynamic aperture length (DAL) correction has been proposed. Using DAL correction, for each reconstruction point $\boldsymbol{r}$, one considers only a subpart of the detection curve $\boldsymbol{S}$ that has constant view angle π from $\boldsymbol{r}$ and where exactly one of the two antipodal detector points is included. Opposed to simply extending the missing data by zero, the DAL correction affects that all singularities are recovered at the correct strength [58, 55, 59].

In this work, we use a further refinement of the DAL correction introduced in [18], which replaces the UBP formula (3) with the more general weighted UBP formula

$$(\mathcal{B}_v g)(\boldsymbol{r}) = \frac{1}{\pi} \int_{\boldsymbol{S}} v(\boldsymbol{r}, \boldsymbol{s}) \Big(\boldsymbol{n}_{\boldsymbol{s}} \cdot (\boldsymbol{r} - \boldsymbol{s}) \int_{|\boldsymbol{r}-\boldsymbol{s}|}^{\infty} \frac{\partial_t t^{-1} g(\boldsymbol{s}, t)}{\sqrt{t^2 - |\boldsymbol{r} - \boldsymbol{s}|^2}} \, \mathrm{d}t \Big) \mathrm{d}\boldsymbol{s} \,. \quad (4)$$

The non-negative weight function $v(\boldsymbol{r}, \boldsymbol{s})$ depending on the reconstruction point $\boldsymbol{r}$ and the detector location $\boldsymbol{s}$ is introduced in such a way that weights for antipodal directions sum up to one. More precisely, the weights satisfy the constraints $v(\boldsymbol{r}, \boldsymbol{s}_+) + v(\boldsymbol{r}, \boldsymbol{s}_-) = 1$ if $\boldsymbol{s}_+, \boldsymbol{s}_- \in \boldsymbol{S}$ are antipodal points and $v(\boldsymbol{r}, \boldsymbol{s}) = 0$ if $\boldsymbol{s} \in \partial \boldsymbol{D} \setminus \boldsymbol{S}$; see Figure 2(b). A particular deterministic choice for the weight function $v(\boldsymbol{r}, \boldsymbol{s})$ has been proposed in [18]. In this paper compute a weight function $v(\boldsymbol{r}, \boldsymbol{s})$ in a data driven manner during the network optimization.

Discretizing (4) yields the approximate left inverse $\mathcal{B}_{\mathbf{V}} \colon \mathbb{R}^{M_s \times M_t} \to \mathbb{R}^{N_r \times N_r}$ accounting for the limited view issue, where $\mathbf{V}$ is a vector including the weights of the DAL. Application of $\mathcal{B}_{\mathbf{V}}$ to the data in (2) accounts for the limited view issue but still yields under-sampling artifacts as well as blurring due the IRF. The limited view issue is accounted by DAL as it recovers all singularities at the correct strength assuming sufficient sampling and ideal IRF. This implies that even in case of limited view data, one has $f = \mathcal{B}\mathcal{W}f + \mathcal{K}f$ in $\boldsymbol{D}$, where $\mathcal{K}$ is at smoothing operator by at least degree one. In the sense of microlocal analysis this means that $\mathcal{B}$ is a parametrix for $\mathcal{W}$ (compare [58]). Under-sampling and blurring due to the IRF will be addressed by combining $\mathcal{B}_{\mathbf{V}}$ with a convolutional neural network and deep learning as described in Section 3.

2.4 Tomographic system

The experimental tomographic system, recently published by Paltauf et.al. [10], was designed for almost real-time PA projection imaging. In brief, the

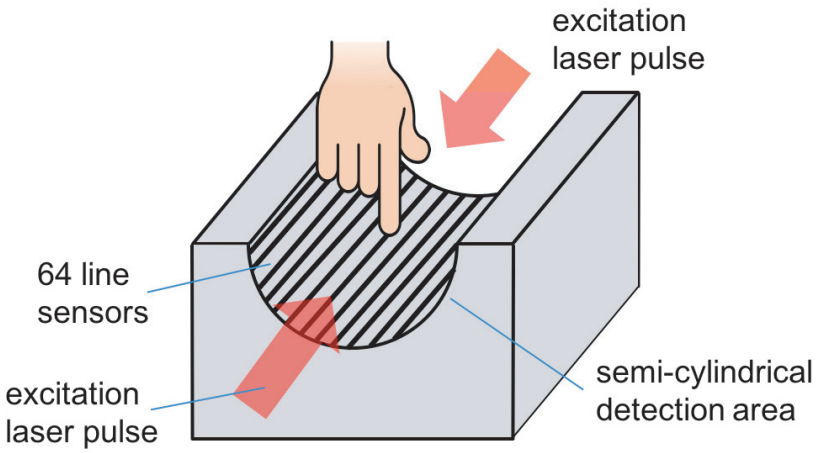


Figure 3: **Schematic illustration of the tomographic system:** The experimental setup contains 64 equispaced piezoelectric line sensors arranged along the detection curve $\boldsymbol{S} = \{\boldsymbol{s} \colon \|\boldsymbol{s}\|_2 = 50\,\text{mm} \wedge \boldsymbol{s}_2 < 0\}$ forming a half-circle, and optical illumination is from two sides.

system is based on piezoelectric polymer film technology with 64 line shaped sensors homogeneously distributed on a semi-cylindrical surface with a diameter of 100 mm, see Figure 3. The width and length of each sensor is 1.5 mm and 150 mm, respectively, and the angular increment between adjacent sensors is 2.8°. The design parameters are steered towards an achievable spatial resolution in the order of 200 µm to 250 µm within an imaging area with radius 20 mm centered on the axis of the cylinder. The choice of a half-cylindrical sensor array arose from considerations regarding the limited-view problem in tomographic reconstruction where all boundaries of an object can be resolved with maximum resolution if the signals are recorded from at least 180° around the object [10]. The readout of the signals is performed with a 32-channel data acquisition device, requiring 2:1 multiplexing for each input. Hence, the projection image acquisition time with the used 20 Hz repetition rate NIR excitation laser system is 0.1 seconds without averaging.

2.5 Data generation

We numerically compute data in (2) at 64 uniformly distributed locations on the detection curve $\boldsymbol{S} = \{\boldsymbol{s} \colon \|\boldsymbol{s}\|_2 = 50\,\text{mm} \wedge \boldsymbol{s}_2 < 0\}$. To generate realistic training data we also include the experimentally found IRF of the used tomographic system. For that purpose we exploit the convolution relation $(\mathcal{A}\mathbf{F}) *_t \boldsymbol{\phi} = \mathcal{A}(\mathbf{F} * \boldsymbol{\Phi})$ derived in [60], which allows applying the point spread function (PSF) $\boldsymbol{\Phi}$ acting in the image domain instead of applying the IRF

ϕ acting in the data domain. The explicit relation between ϕ and $\mathbf{\Phi}$ is computed in [60]. For the present study, this explicit relation is not needed. Instead, we use experimentally measured data $\mathbf{G}_{\text{point}} \simeq \mathcal{A}(\mathbf{F}_{\text{point}}) *_t \phi$ corresponding to a point-like source $\mathbf{F}_{\text{point}}$ to numerically estimate the PSF. Applying the UBP and using the convolution relation yields an approximation of the PSF (or convolution kernel) $\mathbf{\Phi}$.

Having the experimental PSF at hand, noisy data

$$\mathbf{G} = \mathcal{A}(\mathbf{F} * \mathbf{\Phi}) + \boldsymbol{\xi} \tag{5}$$

are computed by convolving the PA source $\mathbf{F}$ with $\mathbf{\Phi}$, solving the wave equation (1) and subsequently adding Gaussian white noise $\boldsymbol{\xi}$ with standard deviation 6 % of the maximum $\max[\mathcal{A}(\mathbf{F} * \mathbf{\Phi})]$ of the exact wave-data.

3 Image reconstruction

3.1 Proposed DALnet

Deep learning is a rapidly emerging research field that has significantly improved performance of many pattern recognition and machine learning applications [61]. Deep learning names special machine learning methods that make use of deep neural network designs for representing a nonlinear input to output map together with optimization procedures for adjusting the weights of the network during the training phase. Recently deep learning algorithms have been developed that give efficient and highly accurate tomographic image reconstruction methods [19, 23, 62, 24, 34, 36, 22, 25, 21, 27]. For tomographic image reconstruction, the task of deep learning is to find an image reconstruction function in the form of a deep network $\mathcal{R}_{\mathbf{W}}$ that maps a measurement data set $\mathbf{G} \in \mathbb{R}^{M_s \times M_t}$ to an output image $\mathbf{F} \in \mathbb{R}^{N_r \times N_r}$. The weight vector $\mathbf{W}$ represents a high dimensional set of free parameters that can be algorithmically adjusted to the particular reconstruction task.

In our case, the input images $\mathbf{G}$ correspond to the noisy measured PA data (2) (or (5)), and the output images $\mathbf{F}$ are the original PA sources evaluated on a discrete grid. The function $\mathcal{R}_{\mathbf{U},\mathbf{V}}$ is an approximate left inverse of the PA forward model, that can be well adapted to a relevant class of PA sources. In this article, we propose a network composed of the UBP with DAL correction to address the limited view issue and a CNN to address under-sampling and the finite IRF. Formally, the proposed reconstruction network (DALnet) has the form

$$\mathcal{R}_{\mathbf{U},\mathbf{V}} = \mathcal{N}_{\mathbf{U}} \circ \mathcal{B}_{\mathbf{V}} \colon \mathbb{R}^{M_s \times M_t} \to \mathbb{R}^{N_r \times N_r}, \tag{6}$$

where

$$\mathcal{B}_{\mathbf{V}}. \colon \mathbb{R}^{M_s \times M_t} \to \mathbb{R}^{N_r \times N_r}$$
$$\mathcal{N}_{\mathbf{U}} \colon \mathbb{R}^{N_r \times N_r} \to \mathbb{R}^{N_r \times N_r}$$

are the discretization of the UBP with DAL correction (4) and the employed CNN, respectively.

The CNN part $\mathcal{N}_{\mathbf{U}}$ can in principle have any network structure. In this work, we use the Unet with residual connection [63, 25, 24, 64] that we describe in more detail in following subsection. The weight vector $[\mathbf{U}, \mathbf{V}] \in \mathbb{R}^p$ is the vector of adjustable parameters in the DALnet (6). The learnable weights $\mathbf{U}$ in the UBP layer correspond to a discretized version of the weight function $v(\boldsymbol{r}, \boldsymbol{s})$. We train the DALnet end-to-end which means that $\mathbf{U}, \mathbf{V}$ are jointly computed during the so-called training phase, see Subsection 3.3. The used DALnet architecture is shown in Figure 4.

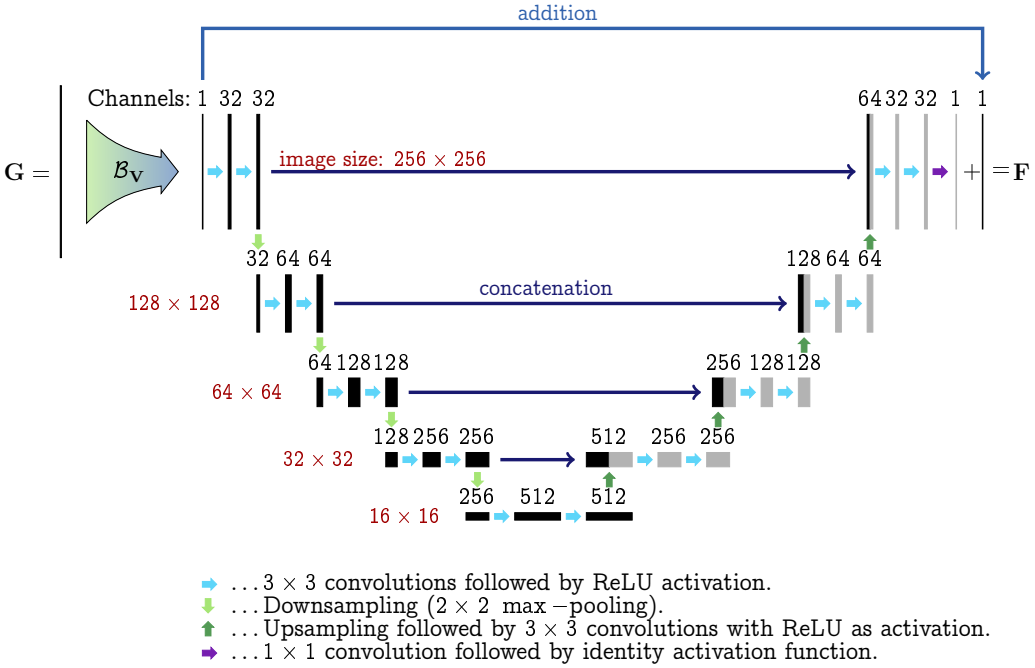


Figure 4: **Architecture of the proposed DALnet.** The first layer $\mathcal{B}_{\mathbf{V}}$ is a UBP with DAL correction and the remaining layers form a Unet $\mathcal{N}_{\mathbf{U}}$ with residual connection. The numbers in red denote the image size, the numbers above the image stacks denote the number of used filters.

3.2 Unet architecture

The employed CNN part of our reconstruction framework consists of a so-called Unet introduced in [63]. Originally, the Unet was designed for biomedical image segmentation and improved versions have recently been used for various image reconstruction tasks [19, 25, 24, 64].

The Unet is a fully convolutional network having a encoder-decoder structure with additional skip connections. The encoder part of the Unet consists of four blocks, where in each block the signal is passed through two convolution layers followed by the rectified linear unit (ReLU) activation function defined by $\mathrm{ReLU}(x) := \max\{x, 0\}$. Due to one max-pooling layer in each block the size of the images decreases while the number of filters increases in every block (see Figure 4). The decoder part of the Unet has the reverse structure, where the downsampling operation (max-pooling) is replaced by a upsampling layer. The skip connections concatenate the interim outputs of the encoder to the upsampled images in the decoder. This prevents the network to lose higher frequency parts of the image, which are lost in the down-sampling and additionally helps passing gradient backwardly, finding better local minima [65]. Further, there is a additive skip connection (residual connection), adding the output of the back-projection at the end since the residual images often have simpler structure and training of such residual networks turned out to be more effective [25].

3.3 Network training

The learning aspect for the proposed reconstruction network DALnet defined by (6) consists in adjusting the parameters $[\mathbf{U}, \mathbf{V}] \in \mathbb{R}^p$ such that $\mathcal{R}_{\mathbf{U},\mathbf{V}}$ performs well on certain classes of real world data. For that purpose, one chooses pairs of so-called training data

$$(\mathbf{G}_n, \mathbf{F}_n) \in \mathbb{R}^{N_r \times N_r} \times \mathbb{R}^{M_s \times M_t} \quad \text{for } n = 1, \ldots, N\,, \tag{7}$$

where $\mathbf{F}_n$ are PA sources and $\mathbf{G}_n$ are the corresponding noisy PA data which are computed according to (5). To measure performance of the reconstruction network one selects an appropriate error function $\mathcal{E}(\mathbf{U}, \mathbf{V})$ that quantifies the overall error made by the network $\mathcal{R}_{\mathbf{U},\mathbf{V}}$ on the training data. During the training phase the weights are adjusted such that the training error $\mathcal{E}(\mathbf{U}, \mathbf{V})$ is minimized.

Several choices for the training error are possible. In the present work, we

use

$$\mathcal{E}(\mathbf{U},\mathbf{V}) \triangleq \frac{1}{2N}\sum_{n=1}^{N} \|\mathcal{R}_{\mathbf{U},\mathbf{V}}(\mathbf{G}_n) - \mathbf{F}_n\|_2^2 \,, \tag{8}$$

defined for all $[\mathbf{U},\mathbf{V}] \in \mathbb{R}^p$ where the entries of $\mathbf{V}$ are non-negative and with $\|\cdot\|_2$ denoting the ℓ^2-norm. Standard methods for minimizing the error function (8) are variants of stochastic or incremental gradient descent algorithms. In this paper we use the stochastic (projected) gradient algorithm with momentum [66, 67], where the momentum parameter and the step size (learning rate) are taken as 0.99 and 10^{-3}, respectively.

3.4 Constraint TV minimization

We compare the proposed DALnet with the UBP, TV-regularization and TV-regularization including a positivity constraint. For (constraint) TV minimization we incorporate the estimated convolution kernel $\boldsymbol{\Phi}$ in the forward operator and construct the output image as a solution of the optimization problem

$$\frac{1}{2}\|\mathcal{A}(\mathbf{F}) * \boldsymbol{\phi} - \mathbf{G}\|_2^2 + \lambda \sum_n \sqrt{|(\mathcal{D}_1\mathbf{F})[n]|^2 + |(\mathcal{D}_2\mathbf{F})[n]|^2} + I_C(\mathbf{F}) \to \min_{\mathbf{F}} \,. \tag{9}$$

Here $\mathcal{D} = [\mathcal{D}_1, \mathcal{D}_2]$ is the discrete gradient operator and λ the regularization parameter, and I_C denotes the indicator of some convex set $C \subseteq \mathbb{R}^{N_r \times N_r}$ defined by $I_C(\mathbf{F}) = 0$ if $\mathbf{F} \in C$ and $I_C(\mathbf{F}) = \infty$ else. In particular, in the case that we take $C = [0,\infty)^{N_r \times N_r}$ it guarantees non-negativity. For $C = \mathbb{R}^{N_r \times N_r}$, (9) reduced to standart TV-regularization.

The discrete TV problem (9) can be minimized by various methods. In this work, we use the minimization algorithm of [68], which is a special instance of the Chambolle-Pock algorithm [69]. The algorithm of [68] for TV minimization has been previously applied to PAT in [70, 71]. However, for PA projection imaging including the detector PSF it is applied for the first time in the present paper.

4 Numerical and experimental results

In this section, we present reconstruction results for UBP, TV-minimization with and without positivity constraint and the proposed DALnet. Results are presented for simulated as well as experimental data.

4.1 Training and evaluation data

Adequate training and evaluation of the network is important in order to perform well on experimental data. For that purpose we generate 200 projection images which are computed from a 3D lung blood vessel data set of size $512 \times 512 \times 512$ by rotating it along a single axis. From these projection images, we extracted 3200 rotated patches $\mathbf{F}_n$ of size 256×256 for training and evaluation. The corresponding data are generated by solving the PAT forward problem according to (5) corresponding to the 64-line array illustrated in Figure 3.

The generated data pairs are split in $N = 3000$ data pairs for training and 200 data pairs for validation. The DALnet is trained by minimizing (8) as described above. All training and evaluation patches are normalized to have a maximal intensity value of one and cover the imaging region $[-12.5\,\text{mm}, 12.5\,\text{mm}] \times [-20\,\text{mm}, 5\,\text{mm}]$ which is mostly contained inside the detection curve $\boldsymbol{S} = \{\boldsymbol{s} \colon \|\boldsymbol{s}\|_2 = 50\,\text{mm} \wedge \boldsymbol{s}_2 < 0\}$.

4.2 Simulation results

Figure 5 shows a comparison of the reconstruction algorithms applied to two randomly chosen examples from evaluation data. The computation time recover a single PA projection image with TV minimization using 30 iterations implemented in Matlab is 48 seconds on a AMD Ryzen 7 1700X CPU. The DALnet is implemented in Keras [72] on top of Tensorflow `https://www.tensorflow.org`. The training was done on a NVIDIA TITAN Xp GPU and lasted for about 10 hours for the whole training procedure. The application of the DALnet (including the learned UBP and the Unet) to one data set only requires 0.018 seconds, and evaluation of the UBP requires 0.013 seconds. This yields to a frame rate of more than 50 reconstructed PA images per second, clearly allowing PA real-time monitoring.

All reconstructions with the UBP show typical angular stripe-like under-sampling artifacts; additionally the results are blurred according to the system PSF. The results for TV-minimization with positivity constraint and the proposed DALnet yield reconstructions almost free from under-sampling artifacts and outperform the other reconstruction methods. Additionally, they are capable to remove (at least partially) the blurring due the the PSF. DALnet even outperforms positivity constraint TV in terms of visual image quality. For TV regularization the regularization parameter has been adjusted manually to yield visually appealing results. The ill-posedness of the involved convolution prohibits decreasing the regularization parameter as

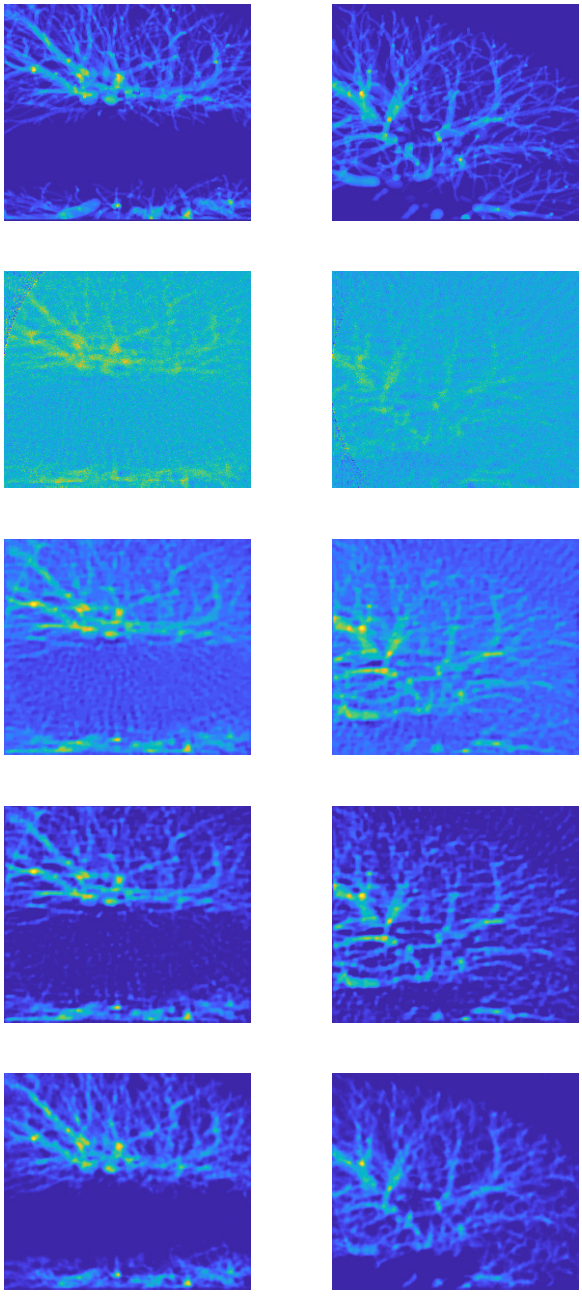


Figure 5: **Reconstructions from (noisy) evaluation data:** First Row: Projection images of lung vessel phantom. Second Row: DAL reconstructions. Third Row: TV-minimization. Fourth Row: TV-minimization with positivity constraint. Bottom Row: Proposed DALnet. The reconstruction region is $[-12.5\,\mathrm{mm}, 12.5\,\mathrm{mm}] \times [-20\,\mathrm{mm}, 5\,\mathrm{mm}]$ and the detection curve is $\boldsymbol{S} = \{\boldsymbol{s}\colon\ \|\boldsymbol{s}\|_2 = 50\,\mathrm{mm} \wedge s_2 < 0\}$.

otherwise the noise turned out to be severely amplified in the reconstruction. The quite large regularization parameter, however, yields to over-smoothing of the fine blood-vessel structures with TV-minimization. The DALnet does not suffer from this limitation and yields high-resolution images without noise amplification.

4.3 Error analysis

For a more quantitative evaluation of the performance of the above reconstruction methods, we evaluate various error measures averaged over the 200 test images not contained in the training data. We evaluate the reconstructions in terms of scaled and shifted relative ℓ^2 and ℓ^1 distance, the scaled and shifted structured similarity index (SSIM; a common measure for predicting the perceived quality of digital images introduced in [73]), and the correlation. Following [24, 33], the scaled and shifted relative ℓ^2 and ℓ^1 distance and scaled and shifted SSIM between two images $\mathbf{H}, \mathbf{F} \in \mathbb{R}^{N_r \times N_r}$ are computed by

$$\begin{aligned}
\mathcal{E}_1(\mathbf{H}, \mathbf{F}) &:= \min_{\alpha,\beta \in \mathbb{R}} \frac{\|\alpha \mathbf{H} - \mathbf{F} - \beta\|_1}{\|\mathbf{F}\|_1}, \\
\mathcal{E}_2(\mathbf{H}, \mathbf{F}) &:= \min_{\alpha,\beta \in \mathbb{R}} \frac{\|\alpha \mathbf{H} - \mathbf{F} - \beta\|_2}{\|\mathbf{F}\|_2}, \\
\mathcal{E}_{\mathrm{SSIM}}(\mathbf{H}, \mathbf{F}) &:= \max_{\alpha,\beta \in \mathbb{R}} \{\mathrm{SSIM}(\alpha \mathbf{H} - \beta, \mathbf{F})\},
\end{aligned}$$

respectively. Here $\|\cdot\|_p$ is the standard ℓ^p distance and SSIM is the structured similarity index. Note that a larger value of $\mathcal{E}_{\mathrm{SSIM}}(\mathbf{H}, \mathbf{F})$ corresponds to a higher structural similarity of $\mathbf{H}$ and $\mathbf{F}$. Opposed to that, smaller values of $\mathcal{E}_2$, $\mathcal{E}_1$ correspond to more similar results.

Table 1 shows the computed error measures for reconstructions with plain UBP, TV, TV with positivity constraint and the proposed DALnet, averaged over 200 test images not contained in the training set. It can be observed that in terms of all error measures DALnet outperforms the other reconstruction measures. Also notably, including positivity significantly improves TV reconstruction in terms of all the quality measures.

4.4 Results for in-vivo data

We also evaluate the reconstruction algorithms on experimental data collected from the 64-line PA system. We therefore have taken several snapshots

error measure	UBP	TV	TV pos	DALnet
ℓ^2	0.555	0.112	0.102	0.085
ℓ^1	0.860	0.418	0.361	0.319
SSIM	0.305	0.586	0.678	0.726
correlation	0.382	0.911	0.919	0.933

Table 1: **Various error measures averaged over 200 test images not contained in the training set.** We evaluate the reconstructions in terms of scaled and shifted relative ℓ^2 and ℓ^1 distances, the scaled and shifted SSIM, and the correlation.

of a finger of one of the authors from 200 different rotation angles around a single axis, and apply the DALnet trained above, the UBP and TV minimization. For TV minimization, we use 30 iterations of the Chambolle-Pock algorithm with the same settings as in the noisy simulated data case. For noise reduction, the PA signals of the human finger are four times averaged prior to the reconstruction process. Two randomly selected reconstructed PA projection images are shown in Figure 6. The reconstructions are again evaluated at 256×256 regular sampling points in the square $[-12.5\,\text{mm}, 12.5\,\text{mm}] \times [-20\,\text{mm}, 5\,\text{mm}]$ with the detector curve $\boldsymbol{S} = \{\boldsymbol{s} \colon \|\boldsymbol{s}\|_2 = 50\,\text{mm} \wedge \boldsymbol{s}_2 < 0\}$.

From Figure 6 one observes that the UBP reconstruction of the finger suffers from streak like under-sampling-artifacts as well as blurring due to the PSF of the PA imaging system. Both, TV minimization and the DALnet are able to partially remove these artifacts. The reconstructions using the DALnet are sharper than the TV reconstructions (with or without positivity constraint) and better capable of removing blurring due to the PSF. In the TV reconstruction, any selection of the regularization parameter λ is a tradeoff between amplifying error and resolving the fine structures of the blood vessels inside the finger. The reconstructions using the DALnet do not suffer from such a trade-off. For TV-minimization (and related variational or iterative algorithms), blood vessel structures and under-sampling artifacts are hardly distinguishable. Increasing the regularization parameter and thereby putting more emphasis on artifact (and noise) removal at the same time also removes fine structures in the blood vessels. Opposed to that, the DALnet is trained to distinguish between blood vessels and under-sampling artifacts and therefore is capable of producing high-resolution reconstructions while also removing under-sampling artifacts.

Following the standard procedure for PAT with integrating line detectors [5, 6, 7], the PA images have been converted to a 3D image $\mathbf{f}_{\text{rec}} \in \mathbb{R}^{N_r \times N_r \times N_r}$ of a finger. Supplementary videos 1-4 (see `https://applied-math.uibk.ac.at/cms/index.php/preprints-2018`) visualize the 3D reconstructions for the

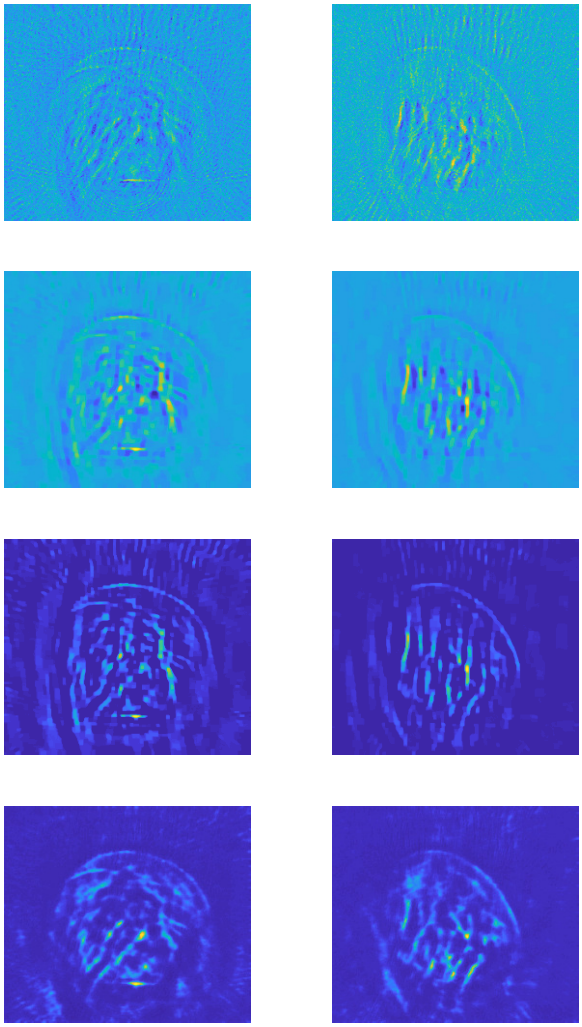


Figure 6: **Reconstructions from experimental data:** Top Row: UBP reconstructions. Second Row: TV-minimization. Third Row: TV-minimization with positivity constraint. Bottom Row: Reconstructions using proposed DALnet. The reconstructions correspond to three different rotation angles; the reconstruction region is $[-12.5\,\text{mm}, 12.5\,\text{mm}] \times [-20\,\text{mm}, 5\,\text{mm}]$; the detectors curve is $\boldsymbol{S} = \{\boldsymbol{s} : \ \|\boldsymbol{s}\|_2 = 50\,\text{mm} \wedge \boldsymbol{s}_2 < 0\}$.

FBP, TV with and without positivity constraint and the proposed DALnet. From these videos DALnet seems to produce the best three dimensional reconstructions of Roberts finger.

5 Conclusion

In this study we reported a deep learning approach for high-resolution PA projection imaging. The proposed DALnet seems to be the first network for PAT that is capable to account for limited view, under-sampling artifacts and blurring due the system PSF. We designed and trained the DALnet for a piezoelectric 64-line detector system [10]. The obtained direct reconstruction algorithm requires less that 1/50 seconds on a standard desktop PC in with an NVIDIA TITAN Xp GPU (available for about 1400 euro) to reconstruct a 256×256 PA projection image. We are not aware of any PAT system that is capable to produce such high-resolution real-time monitoring of 3D structures at such low hardware costs.

Future work will be done to compare the proposed DALnet with other deep learning image reconstruction approaches including the null-space network [31], iterative networks [32, 34], learned projected gradient [35], variational networks [36] and the learned network regularizers [74]. Particular emphasis will be given on the evaluation on real world data. Finally, we point out that the proposed network is not restricted to PA imaging. The design of similar networks for other tomographic modalities is possible and subject of future investigations. This includes fan beam and spiral CT, where weight corrections are inherently included in FPB algorithms that are still standard in commercial CT scanners.

Acknowledgement

SA and MH acknowledge support of the Austrian Science Fund (FWF), project P 30747-N32. The work of RN has been supported by the FWF, project P 28032. JS, SA and MH acknowledge support of NVIDIA Corporation with the donation of the Titan Xp GPU used for this research.

References

[1] P. Beard, "Biomedical photoacoustic imaging," *Interface focus*, vol. 1, no. 4, pp. 602–631, 2011.

[2] L. V. Wang, "Multiscale photoacoustic microscopy and computed tomography," *Nature Phot.*, vol. 3, no. 9, pp. 503–509, 2009.

[3] P. Burgholzer, C. Hofer, G. Paltauf, M. Haltmeier, and O. Scherzer, "Thermoacoustic tomography with integrating area and line detectors," *IEEE Trans. Ultrasonic and Frequency Control*, vol. 52, no. 9, pp. 1577–1583, September 2005.

[4] G. Paltauf, R. Nuster, M. Haltmeier, and P. Burgholzer, "Photoacoustic tomography using a Mach-Zehnder interferometer as an acoustic line detector," *App. Opt.*, vol. 46, no. 16, pp. 3352–3358, 2007.

[5] P. Burgholzer, J. Bauer-Marschallinger, H. Grün, M. Haltmeier, and G. Paltauf, "Temporal back-projection algorithms for photoacoustic tomography with integrating line detectors," *Inverse Probl.*, vol. 23, no. 6, pp. S65–S80, 2007.

[6] M. Haltmeier, "Frequency domain reconstruction for photo- and thermoacoustic tomography with line detectors," *Math. Models Methods Appl. Sci.*, vol. 19, no. 2, pp. 283–306, 2009.

[7] G. Paltauf, R. Nuster, M. Haltmeier, and P. Burgholzer, "Photoacoustic tomography with integrating area and line detectors," in *Photoacoustic imaging and spectroscopy*. CRC Press, 2009, ch. 20, pp. 251–263.

[8] S. Gratt, R. Nuster, G. Wurzinger, M. Bugl, and G. Paltauf, "64-line-sensor array: fast imaging system for photoacoustic tomography," *Proc. SPIE*, vol. 8943, p. 894365, 2014.

[9] J. Bauer-Marschallinger, K. Felbermayer, K.-D. Bouchal, I. A. Veres, H. Grün, P. Burgholzer, and T. Berer, "Photoacoustic projection imaging using a 64-channel fiber optic detector array," in *Proc. SPIE*, vol. 9323, 2015.

[10] G. Paltauf, P. Hartmair, G. Kovachev, and R. Nuster, "Piezoelectric line detector array for photoacoustic tomography," *Photoacoustics*, vol. 8, pp. 28–36, 2017.

[11] J. Bauer-Marschallinger, K. Felbermayer, and T. Berer, "All-optical photoacoustic projection imaging," *Biomed. Opt. Express*, vol. 8, no. 9, pp. 3938–3951, 2017.

[12] S. Arridge, P. Beard, M. Betcke, B. Cox, N. Huynh, F. Lucka, O. Ogunlade, and E. Zhang, "Accelerated high-resolution photoacoustic tomography via compressed sensing," *Phys. Med. Biol.*, vol. 61, no. 24, p. 8908, 2016.

[13] M. Haltmeier, T. Berer, S. Moon, and P. Burgholzer, "Compressed sensing and sparsity in photoacoustic tomography," *J. Opt.*, vol. 18, no. 11, pp. 114 004–12pp, 2016.

[14] M. Haltmeier, M. Sandbichler, T. Berer, J. Bauer-Marschallinger, P. Burgholzer, and L. Nguyen, "A new sparsification and reconstruction strategy for compressed sensing photoacoustic tomography," *arXiv:1801.00117*, 2017.

[15] M. Sandbichler, F. Krahmer, T. Berer, P. Burgholzer, and M. Haltmeier, "A novel compressed sensing scheme for photoacoustic tomography," *SIAM J. Appl. Math.*, vol. 75, no. 6, pp. 2475–2494, 2015.

[16] J. Provost and F. Lesage, "The application of compressed sensing for photo-acoustic tomography," *IEEE Trans. Med. Imag.*, vol. 28, no. 4, pp. 585–594, 2009.

[17] G. Paltauf, R. Nuster, M. Haltmeier, and P. Burgholzer, "Experimental evaluation of reconstruction algorithms for limited view photoacoustic tomography with line detectors," *Inverse Probl.*, vol. 23, no. 6, pp. S81–S94, 2007.

[18] G. Paltauf, R. Nuster, and P. Burgholzer, "Weight factors for limited angle photoacoustic tomography," *Phys. Med. Biol.*, vol. 54, no. 11, p. 3303, 2009.

[19] S. Antholzer, M. Haltmeier, and J. Schwab, "Deep learning for photoacoustic tomography from sparse data," *arXiv:1704.04587*, 2017, to appear in Inverse Probl Sci Eng.

[20] D. M. Pelt and K. J. Batenburg, "Improving filtered backprojection reconstruction by data-dependent filtering," *IEEE Trans. Image Process.*, vol. 23, no. 11, pp. 4750–4762, 2014.

[21] G. Wang, "A perspective on deep imaging," *IEEE Access*, vol. 4, pp. 8914–8924, 2016.

[22] S. Wang, Z. Su, L. Ying, X. Peng, S. Zhu, F. Liang, D. Feng, and D. Liang, "Accelerating magnetic resonance imaging via deep learning," in *IEEE 13th International Symposium on Biomedical Imaging (ISBI)*, 2016, pp. 514–517.

[23] H. Chen, Y. Zhang, W. Zhang, P. Liao, K. Li, J. Zhou, and G. Wang, "Low-dose CT via convolutional neural network," *Biomed. Opt. Express*, vol. 8, no. 2, pp. 679–694, 2017.

[24] K. H. Jin, M. T. McCann, E. Froustey, and M. Unser, "Deep convolutional neural network for inverse problems in imaging," *IEEE Trans. Image Process.*, vol. 26, no. 9, pp. 4509–4522, 2017.

[25] Y. Han, J. J. Yoo, and J. C. Ye, "Deep residual learning for compressed sensing CT reconstruction via persistent homology analysis," *arXiv:1611.06391 [cs.CV]*, 2016.

[26] T. Würfl, F. C. Ghesu, V. Christlein, and A. Maier, "Deep learning computed tomography," in *International Conference on Medical Image Computing and Computer-Assisted Intervention*. Springer, 2016, pp. 432–440.

[27] H. Zhang, L. Li, K. Qiao, L. Wang, B. Yan, L. Li, and G. Hu, "Image prediction for limited-angle tomography via deep learning with convolutional neural network," arXiv:1607.08707, 2016.

[28] Y. Rivenson, Z. Göröcs, H. Günaydin, Y. Zhang, H. Wang, and A. Ozcan, "Deep learning microscopy," *Optica*, vol. 4, no. 11, pp. 1437–1443, 2017.

[29] S. Antholzer, M. Haltmeier, R. Nuster, and J. Schwab, "Photoacoustic image reconstruction via deep learning," in *Photons Plus Ultrasound: Imaging and Sensing 2018*, vol. 10494. International Society for Optics and Photonics, 2018, p. 104944U.

[30] D. Allman, A. Reiter, and M. A. L. Bell, "Photoacoustic source detection and reflection artifact removal enabled by deep learning," *IEEE Trans. Med. Imaging*, vol. 37, no. 6, pp. 1464–1477, 2018.

[31] J. Schwab, S. Antholzer, and M. Haltmeier, "Deep null space learning for inverse problems: Convergence analysis and rates," *arXiv:1806.06137*, 2018.

[32] J. Adler and O. Öktem, "Solving ill-posed inverse problems using iterative deep neural networks," *arXiv:1704.04058*, 2017.

[33] A. Hauptmann, F. Lucka, M. Betcke, N. Huynh, J. Adler, B. Cox, P. Beard, S. Ourselin, and S. Arridge, "Model-based learning for accelerated, limited-view 3-d photoacoustic tomography," *IEEE Trans. Med. Imaging*, vol. 37, no. 6, pp. 1382–1393, 2018.

[34] B. Kelly, T. P. Matthews, and M. A. Anastasio, "Deep learning-guided image reconstruction from incomplete data," *arXiv:1709.00584*, 2017.

[35] H. Gupta, K. H. Jin, H. Q. Nguyen, M. T. McCann, and M. Unser, "Cnn-based projected gradient descent for consistent ct image reconstruction," *IEEE Trans. Med. Imag.*, vol. 37, no. 6, pp. 1440–1453, 2018.

[36] E. Kobler, T. Klatzer, K. Hammernik, and T. Pock, "Variational networks: connecting variational methods and deep learning," in *German Conference on Pattern Recognition*. Springer, 2017, pp. 281–293.

[37] D. Waibel, J. Gröhl, F. Isensee, T. Kirchner, K. Maier-Hein, and L. Maier-Hein, "Reconstruction of initial pressure from limited view photoacoustic images using deep learning," in *Photons Plus Ultrasound: Imaging and Sensing 2018*, vol. 10494. International Society for Optics and Photonics, 2018, p. 104942S.

[38] M. Xu and L. V. Wang, "Analytic explanation of spatial resolution related to bandwidth and detector aperture size in thermoacoustic or photoacoustic reconstruction," *Phys. Rev. E*, vol. 67, no. 5, pp. 0 566 051–05 660 515 (electronic), 2003.

[39] M. Haltmeier and G. Zangerl, "Spatial resolution in photoacoustic tomography: Effects of detector size and detector bandwidth," *Inverse Probl.*, vol. 26, no. 12, p. 125002, 2010.

[40] M. Haltmeier, "Sampling conditions for the circular radon transform," *IEEE Trans. Image Process.*, vol. 25, no. 6, pp. 2910–2919, 2016.

[41] P. Burgholzer, G. J. Matt, M. Haltmeier, and G. Paltauf, "Exact and approximate imaging methods for photoacoustic tomography using an arbitrary detection surface," *Phys. Rev. E*, vol. 75, no. 4, p. 046706, 2007.

[42] B. E. Treeby and B. T. Cox, "k-wave: Matlab toolbox for the simulation and reconstruction of photoacoustic wave-fields," *J. Biomed. Opt.*, vol. 15, p. 021314, 2010.

[43] Y. Hristova, P. Kuchment, and L. Nguyen, "Reconstruction and time reversal in thermoacoustic tomography in acoustically homogeneous and inhomogeneous media," *Inverse Probl.*, vol. 24, no. 5, p. 055006 (25pp), 2008.

[44] D. Finch, M. Haltmeier, and Rakesh, "Inversion of spherical means and the wave equation in even dimensions," *SIAM J. Appl. Math.*, vol. 68, no. 2, pp. 392–412, 2007.

[45] M. Haltmeier, "Universal inversion formulas for recovering a function from spherical means," *SIAM J. Math. Anal.*, vol. 46, no. 1, pp. 214–232, 2014.

[46] ——, "Inversion of circular means and the wave equation on convex planar domains," *Comput. Math. Appl.*, vol. 65, no. 7, pp. 1025–1036, 2013.

[47] L. A. Kunyansky, "Explicit inversion formulae for the spherical mean Radon transform," *Inverse Probl.*, vol. 23, no. 1, pp. 373–383, 2007.

[48] P. Kuchment and L. Kunyansky, "Mathematics of thermoacoustic tomography," *Eur. J. Appl. Math.*, vol. 19, no. 2, pp. 191–224, 2008.

[49] A. Rosenthal, V. Ntziachristos, and D. Razansky, "Acoustic inversion in optoacoustic tomography: A review," *Curr. Med. Imaging Rev.*, vol. 9, no. 4, pp. 318–336, 2013.

[50] M. Xu and L. V. Wang, "Universal back-projection algorithm for photoacoustic computed tomography," *Phys. Rev. E*, vol. 71, no. 1, p. 016706, 2005.

[51] P. Burgholzer, J. Bauer-Marschallinger, H. Grün, M. Haltmeier, and G. Paltauf, "Temporal back-projection algorithms for photoacoustic tomography with integrating line detectors," *Inverse Probl.*, vol. 23, no. 6, pp. S65–S80, 2007.

[52] M. Haltmeier and S. Pereverzyev, Jr., "The universal back-projection formula for spherical means and the wave equation on certain quadric hypersurfaces," *J. Math. Anal. Appl.*, vol. 429, no. 1, pp. 366–382, 2015.

[53] F. Natterer, "Photo-acoustic inversion in convex domains," *Inverse Probl. Imaging*, vol. 6, no. 2, pp. 315–320, 2012.

[54] X. L. Dean-Ben, A. Buehler, V. Ntziachristos, and D. Razansky, "Accurate model-based reconstruction algorithm for three-dimensional optoacoustic tomography," *IEEE Trans. Med. Imag.*, vol. 31, no. 10, pp. 1922–1928, 2012.

[55] M. Haltmeier and L. V. Nguyen, "Analysis of iterative methods in photoacoustic tomography with variable sound speed," *SIAM J. Imaging Sci.*, vol. 10, no. 2, pp. 751–781, 2017.

[56] G. Paltauf, J. A. Viator, S. A. Prahl, and S. L. Jacques, "Iterative reconstruction algorithm for optoacoustic imaging," *J. Opt. Soc. Am.*, vol. 112, no. 4, pp. 1536–1544, 2002.

[57] K. Wang, R. Su, A. A. Oraevsky, and M. A. Anastasio, "Investigation of iterative image reconstruction in three-dimensional optoacoustic tomography," *Phys. Med. Biol.*, vol. 57, no. 17, p. 5399, 2012.

[58] L. V. Nguyen, "On a reconstruction formula for spherical radon transform: a microlocal analytic point of view," *Anal. Math. Phys.*, vol. 4, no. 3, pp. 199–220, 2014.

[59] P. Stefanov and G. Uhlmann, "Thermoacoustic tomography with variable sound speed," *Inverse Probl.*, vol. 25, no. 7, pp. 075 011, 16, 2009.

[60] M. Haltmeier and G. Zangerl, "Spatial resolution in photoacoustic tomography: effects of detector size and detector bandwidth," *Inverse Probl.*, vol. 26, no. 12, p. 125002, 2010.

[61] I. Goodfellow, Y. Bengio, and A. Courville, *Deep Learning*. MIT Press, 2016.

[62] Y. Han, J. Gu, and J. C. Ye, "Deep learning interior tomography for region-of-interest reconstruction," *arXiv:1712.10248*, 2017.

[63] O. Ronneberge, P. Fischer, and T. Brox, "U-net: Convolutional networks for biomedical image segmentation," in *International Conference on Medical Image Computing and Computer-Assisted Intervention*, 2015, pp. 234–241.

[64] J. C. Ye, Y. Han, and E. Cha, "Deep convolutional framelets: A general deep learning framework for inverse problems," *SIAM J. Imaging Sci.*, vol. 11, no. 2, pp. 991–1048, 2018.

[65] X. Mao, C. Shen, and Y. Yang, "Image restoration using very deep convolutional encoder-decoder networks with symmetric skip connections," in *Advances in neural information processing systems*, 2016, pp. 2802–2810.

[66] O. L. Mangasarian and M. V. Solodov, "Backpropagation convergence via deterministic nonmonotone perturbed minimization," in *Advances in Neural Information Processing Systems*, 1994, pp. 383–390.

[67] P. Tseng, "An incremental gradient (-projection) method with momentum term and adaptive stepsize rule," *SIAM J. Optim.*, vol. 8, no. 2, pp. 506–531, 1998.

[68] E. Y. Sidky, J. H. Jørgensen, and X. Pan, "Convex optimization problem prototyping for image reconstruction in computed tomography with the chambolle–pock algorithm," *Phys. Med. Biol.*, vol. 57, no. 10, p. 3065, 2012.

[69] A. Chambolle and T. Pock, "A first-order primal-dual algorithm for convex problems with applications to imaging," *J. Math. Imaging Vision*, vol. 40, no. 1, pp. 120–145, 2011.

[70] Y. E. Boink, M. J. Lagerwerf, W. Steenbergen, S. A. van Gils, S. Manohar, and C. Brune, "A framework for directional and higher-order reconstruction in photoacoustic tomography," *Phys. Med. & Biol.*, vol. 63, no. 4, p. 045018, 2018.

[71] L. V. Nguyen and M. Haltmeier, "Reconstruction algorithms for photoacoustic tomography in heterogenous damping media," 2018, preprint.

[72] F. Chollet, "Keras," https://github.com/fchollet/keras, 2015, gitHub.

[73] Z. Wang, A. C. Bovik, H. R. S., and E. P. Simoncelli, "Image quality assessment: from error visibility to structural similarity," *IEEE Trans Image Process*, vol. 13, no. 4, pp. 600–612, 2004.

[74] H. Li, J. Schwab, S. Antholzer, and M. Haltmeier, "NETT: Solving inverse problems with deep neural networks," *arXiv:1803.00092*, 2018.